Zusammenfassung

Wir verwenden Computersimulationen, um die Selbstdiffusion von hantelförmigen Teilchen in zweidimensionalen Flüssigkeiten mit hoher Teilchenkonzentration zu untersuchen. Wir untersuchen den Einfluss des Füllungsgrades ϕ und der Struktur des Teilchens auf die Diffusionseigenschaften. Wir berechnen die zeitlich gemittelte mittlere quadratische Verschiebung (MSD), die Verschiebungswahrscheinlichkeitsdichtefunktion (PDF) und die Verschiebungsautokorrelationsfunktion der Teilchen und vergleichen unsere Ergebnisse mit denen einer ähnlichen Untersuchung sternförmiger Teilchen [1]. Das System weist zwei unterschiedliche Diffusionsregime auf, die sich durch den Skalierungsexponenten des MSDs, die Abhängigkeit des Diffusionskoeffizienten von ϕ und die Verschiebungsautokorrelationsfunktion unterscheiden. Wir führen den Regimewechsel auf den Übergang von einer viskosen zu einer viskoelastischen Flüssigkeit zurück. Wir zeigen auch, dass die Schwingung der Partikel durch steigende ϕ unterdrückt wird. Hohe Füllungsgrade führen zu nicht-gaußförmigen PDFs. Unsere Ergebnisse könnten verwendet werden, um Vorhersagen über die Diffusionseigenschaften von Teilchen mit einfacher Struktur zu machen.

Abstract

We use computer simulations to study the self-diffusion of dumbbell-shaped particles in crowded two-dimensional liquids. We investigate the effect of the crowding fraction ϕ and the structure of the particle on the diffusion properties. We evaluate the time-averaged mean squared displacement (MSD), the displacement probability density function (PDF) and the displacement autocorrelation function of the particles and compare them to a similar study of star-shaped particles [1]. The system exhibits two different diffusion regimes distinguished by the scaling exponent of the MSD, the dependence of the diffusivity on ϕ and the displacement autocorrelation function. We attribute the change of regimes to a crowded induced transition from a viscous to a viscoelastic liquid. Also, we show that the vibration of the particles is suppressed by the crowding. High crowding fractions give rise to non-Gaussian PDFs. Our findings could be used to make predictions about the diffusion properties of simple crowders.

Contents

1 Introduction

In 1827, botanist Robert Brown observed under a microscope the erratic and random motion of particles ejected from pollen suspended in water [2]. About 80 years later, Albert Einstein [3] came up with the theoretical description for this Brownian motion. He derived the diffusion equation for a particle density under three assumptions. First, the motion of a diffusing particle is independent from the motion of all other diffusing particles. Second, the motions of a single particle in different time intervals are also independent from each other. Third, the motion is symmetric in all directions. The solution of the diffusion equation for a single particle starting at $x(0) = 0$ is the Gaussian PDF

$$p(x,t) = \frac{n}{\sqrt{4\pi D t}}\, \mathrm{e}^{\frac{-x^2}{4Dt}}, \tag{1.1}$$

where D is the diffusivity, x the position and t the time. Einstein then calculated the second moment of this PDF, also known as the mean-squared displacement,

$$\langle x^2(t) \rangle = 2Dt. \tag{1.2}$$

The diffusion that arises from a motion that satisfies equations 1.1 and 1.2 is called standard Brownian diffusion. In addition, Einstein derived a relation linking the diffusivity of a spherical particle to the temperature T, the viscosity η of the liquid and the radius of the particle P

$$D = \frac{k_B T}{6\pi\eta P} = \frac{k_B T}{\gamma}. \tag{1.3}$$

Here $\gamma = 6\pi\eta P$ denotes the damping constant. Marian Smoluchowski independently derived similar relations [4]. Hence, equation 1.3 is known as the Einstein-Smulochowski relation.
In 1908, Paul Langevin derived equations 1.2 and 1.3 using a different approach [5]. Starting from Newton's second law, he used Stokes' drag and introduced a random force ξ to set up a differential equation

$$m\frac{\mathrm{d}^2 x(t)}{\mathrm{d}t^2} = -\gamma\frac{\mathrm{d}x(t)}{\mathrm{d}t} + \xi(t). \tag{1.4}$$

Today, this differential is known as the Langevin equation. Langevin made assumptions about ξ that are equivalent to Einstein's. A random force that satisfies these assumptions is called white Gaussian noise. Langevin's formulation of Brownian motion takes the inertia of the particle into account. Thus, it can describe the short-time behaviour of

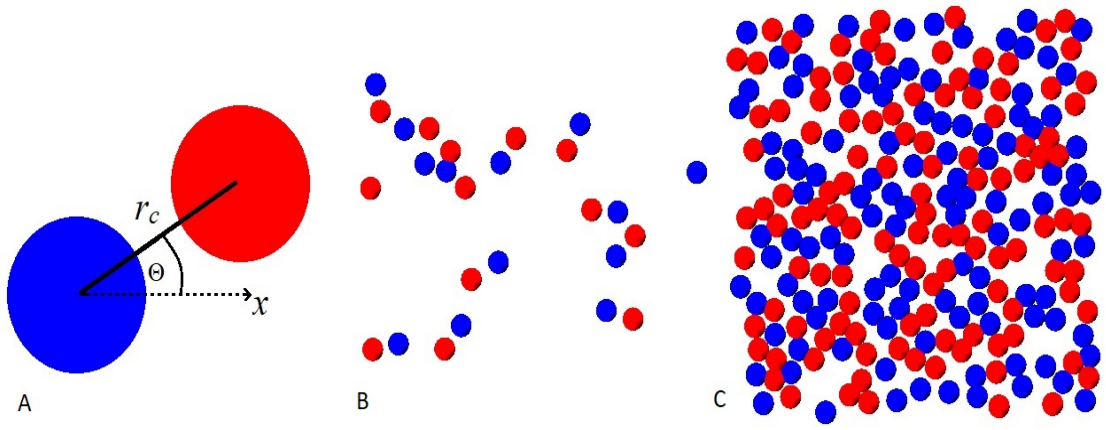

Figure 1.1: A: Dumbbell-shaped dimer. B: Diluted system at $\phi = 0.05$. C: Highly crowded system at $\phi = 0.45$.

the particle before diffusion sets in [6].

In recent years, deviations from standard Brownian motion have been observed in a range of different systems. This anomalous diffusion is characterised by a generalisation of equation 1.2

$$\langle x^2(t)\rangle = 2D_\beta t^\beta, \tag{1.5}$$

with a generalised diffusivity D_β and the scaling exponent β. For $\beta = 1$, equation 1.2 is recovered. For $0 < \beta < 1$, the motion the called subdiffusive and superdiffusive for $\beta > 1$. Superdiffusion has been found in the cytoplasm of Acanthamoebae and was attributed to active motion caused by myosin II motors and cell locomotion [7]. Conversely, subdiffusion is associated with passive motion in crowded environments such as cytoplasm, in which crowding can reach values of $\phi \sim 0.3$ [8].

From a conceptual perspective, crowding is an obvious reason for anomalous diffusion as an increased particle density causes more collisions between the diffusing particles. Hence, the motion of different crowders cannot be seen as independent as assumed by Einstein. Consequently, new models have been proposed to describe anomalous diffusion [9]. These model include, among others, continuous time random walk [10], fractional Brownian motion [11] and fractional Langevin equation [12], scaled Brownian motion [13] and heterogeneous diffusion processes [14]. Similar to the diversity of anomalous diffusion phenomena, numerous models exists and in a particular system multiple models combined are used to describe the properties of the diffusion.

In non-biological colloidal systems, the crowding can reach even higher values leading to a transition from a liquid to a amorphous solid, a glass transition [15]. In addition, crowding has been shown to impede or felicitate polymer looping based on the size of the crowders [16].

The dumbbell-shaped dimer (1.1) is the simplest example of a linear polymer crowder. Thus, the effect of an additional particle interaction, compared to single colloidal parti-

cles, can be examined. In comparison to diffusion of star-shaped crowders [1], the effects of the complexity of the crowder structure can be elucidated.

2 Model and Simulation

2.1 Physical model

In our model, we consider two-dimensional dumbbell-shaped dimers suspended in a liquid. Each dimer, see figure 1.1, consists of two monomer disks of diameter σ that are hold together by an elastic spring. The harmonic potential between the disks is

$$U_h(r) = \frac{1}{2}k\left(r - r_0\right)^2, \tag{2.1}$$

where $r_0 = 1.5\sigma$ is the equilibrium distance and $k = 100k_BT/\sigma^2$ the spring constant. Here k_B denotes the Boltzmann constant and T the absolute temperature.

In addition, a Lennard-Jones Potential acts between all disks

$$U_{\mathrm{LJ}}(r) = 4\epsilon\left[-\left(\frac{\sigma}{r}\right)^6 + \left(\frac{\sigma}{r}\right)^{12}\right]. \tag{2.2}$$

The $(\frac{\sigma}{r})^{12}$ term models the hardness of the disks as it diverges quickly for $r < \sigma$. The $-(\frac{\sigma}{r})^6$ term provides a weak attraction between the disks and thus between the dimers. ϵ determines the maximal strength of this attraction present at $r = 2^{1/6}\sigma \approx 1.12\sigma$. In our model we use $\epsilon = 1k_BT$.

Accounting for the forces resulting from these potentials, the Langevin equation for the position of the ith monomer disk $\mathbf{r}_i$ is

$$m\frac{\mathrm{d}^2\mathbf{r}_i(t)}{\mathrm{d}t^2} = -\gamma\frac{\mathrm{d}\mathbf{r}_i(t)}{\mathrm{d}t} - \sum_{\substack{j=1\\ j\neq i}}^{N}\nabla\big(U_{\mathrm{LJ}}(r_{ij})\big)\Theta(2\sigma - r) - \nabla U_h(r_{ik}) + \xi_i(t). \tag{2.3}$$

$\xi(t)$ denotes Gaussian white noise with zero mean $\overline{\xi(t)} = 0$ and correlation $\overline{\xi(t)\xi(t')} = 4\gamma k_BT\delta(t - t')$, with γ the friction coefficient. The noise has two independent components for each of the Cartesian coordinates.

All dimers are confined in a square box of area L^2. However, we use periodic boundary conditions, to allow for an unconfined motion of the dimers. The crowding in the box for N dimers is quantified by the packing fraction ϕ

$$\phi = \frac{NA}{L^2}. \tag{2.4}$$

Here $A = 2\cdot\pi(\frac{\sigma}{2})^2$ is the area of a dimer. In our study, the system size is $L = 20\sigma$. The used N and corresponding ϕ can be seen in table 2.1.

N	1	13	38	63	89	115	140	166
ϕ	0.004	0.05	0.15	0.25	0.35	0.45	0.55	0.65

Table 2.1: Used number of dimers N and corresponding packing fractions ϕ

2.2 Simulation

We simulate the system by solving equation 2.3 numerically using the Verlet velocity algorithm.

$$x_i(t+\Delta t) = \frac{1}{2}a_{i,x}(t)\Delta t^2 + v_{i,x}(t)\Delta t + x_i(t) \tag{2.5}$$

$$v_{i,x}(t+\Delta t) = \frac{a_{i,x}(t) + a_{i,x}(t+\Delta t)}{2}\Delta t + v_{i,x}(t), \tag{2.6}$$

with the integration time step $\Delta t = 0.005$. For the acceleration $a_x(t)$ we use the forces stemming from the interaction potentials from equation 2.3

$$a_x(t) = \left(-\sum_{\substack{j=1 \\ j\neq i}}^{N} \nabla U_{\mathrm{LJ}}(r_{ij}) - \nabla U_h(r_{ik}) \right)_x . \tag{2.7}$$

Friction is considered according to [17] as γ-dependent coefficients and the noise is modelled by correlated random displacements $\xi_x(t)$ and $\xi_{v_x}(t)$

$$x_i(t+\Delta t) = c_{x1}(\Delta t,\gamma)a_{i,x}(t) + c_{x2}(\Delta t,\gamma)v_{i,x}(t) + x_i(t) + \xi_x(t) \tag{2.8}$$

$$v_{i,x}(t+\Delta t) = c_{v1}(\Delta t,\gamma)a_{i,x}(t) + c_{v2}(\Delta t,\gamma)a_{i,x}(t+\Delta t) + c_{v3}(\Delta t,\gamma)v_{i,x}(t) + \xi_{v_x}(t), \tag{2.9}$$

with

$$c_{x1} = \frac{\gamma\Delta t - 1 - \mathrm{e}^{-\gamma\Delta t}}{\gamma^2} \tag{2.10}$$

$$c_{x2} = \frac{1 - \mathrm{e}^{-\gamma\Delta t}}{\gamma} \tag{2.11}$$

$$c_{v1} = \frac{1 - \mathrm{e}^{-\gamma\Delta t}}{\gamma} + \frac{1 - \mathrm{e}^{-\gamma\Delta t}}{\gamma^2\Delta t} + \frac{1}{\gamma} \tag{2.12}$$

$$c_{v2} = \frac{\gamma\Delta t - 1 - \mathrm{e}^{-\gamma\Delta t}}{\gamma^2\Delta t} \tag{2.13}$$

$$c_{v3} = \mathrm{e}^{-\gamma\Delta t}. \tag{2.14}$$

In the limit $\gamma \to 0$, the coefficients of equations 2.5 and 2.6 are recovered. We set γ to unity in our simulations.

The simulated trace length is $T_{sim} = 10^8 \Delta t$. To give Δt a physical meaning, we use the standard combination [17]

$$200\Delta t = \delta\tau = \sigma\sqrt{\frac{m}{k_B T}} \approx 1\,\text{ns}, \tag{2.15}$$

with the disk diameter set to $\sigma = 6\,\text{ns}$, the mass estimated by the average mass of crowders in the nucleolus [18] $m \approx 68\,\text{kDa}$ and the temperature $T = 272.15\,\text{K}$. Thus, the simulated trace length in physical time is $T_{sim} = 0.5\,\text{ms}$. In the following, all times are expressed in units of $\delta\tau$.

The simulation runs for a time T_{eq} before the measurement starts, see figure 2.1. In order to exceed the relaxation time of the crowders T_{cr} by two orders of magnitude, the equilibration time is set to $2 \cdot 10^4$ for all ϕ. For T_{cr}, we use the estimation from [1]

$$T_{cr} = \Big(R_{cr}/\sigma\Big)^2 \Big/ D_{avg}, \tag{2.16}$$

where R_{cr} denotes the radius of the dimer and D_{avg} its average diffusivity.

After T_{eq}, we measure four observables of every dimer, the x and y coordinates of the centre of mass of the dimers $x_c(t)$ and $y_c(t)$, the angle $\Theta(t)$ between the dimer and the x axis, see fig, and the relative distance between the monomer disks within a dimer $d(t)$.

Figure 2.1 shows a simplified flow chart of the simulation. After the initial set up of the system, the integration loop is executed. In this loop, equations 2.8 and 2.9 are repeatedly evaluated. The full source code can be found at [19].

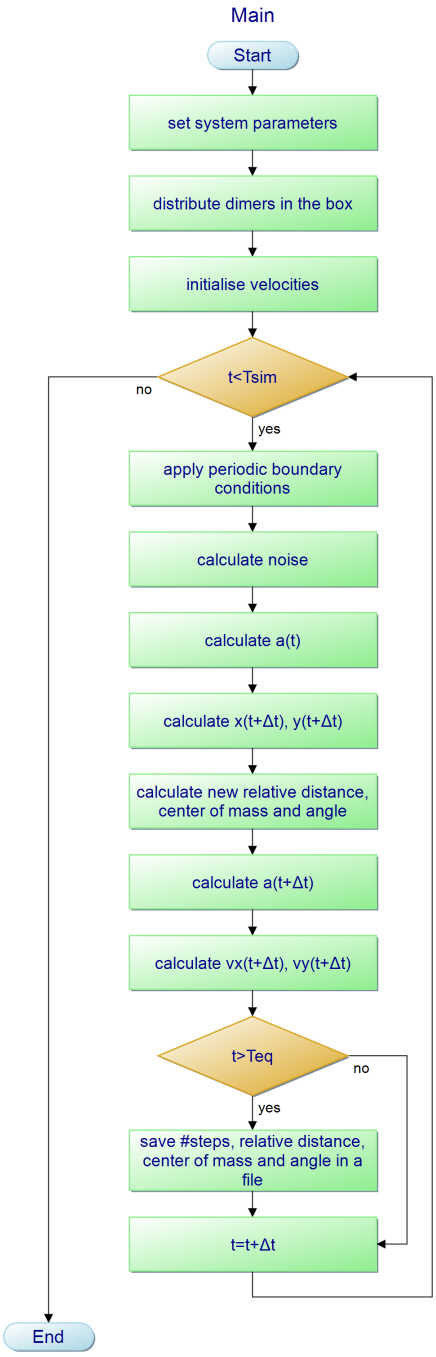

Figure 2.1: Simple flow chart of the simulation consisting of a system initialisation and an integration loop

3 Results

We use three approaches to analyse the data gained form the simulations to examine the diffusion properties of the dumbbell-shaped dimers. First, we calculate and analyse the time-averaged MSD. Second, the displacement probability density function is investigated. Third, various displacement autocorrelation functions are computed. The displacement δ is the difference between two values of an observable at two times separated by the lag time Δ

$$\delta_x(t,\Delta) = x_c(t+\Delta) - x_c(t) \tag{3.1}$$
$$\delta_y(t,\Delta) = y_c(t+\Delta) - y_c(t) \tag{3.2}$$
$$\delta_r(t,\Delta) = \Theta(t+\Delta) - \Theta(t) \tag{3.3}$$
$$\delta_d(t,\Delta) = d(t+\Delta) - d(t). \tag{3.4}$$

In the following, only the results for δ_x are shown for the linear motion as δ_y displays the same behaviour.

3.1 Time-averaged mean squared displacement

We begin by investigating the time-averaged MSD. First, we compute the translational $\overline{\delta_i}$ and rotational $\overline{\delta_{r,i}}$ MSD of the ith dimer as [9]

$$\overline{\delta^2_{i,x}(\Delta)} = \frac{1}{T-\Delta}\int_0^{T-\Delta} \delta^2_{i,x}(t,\Delta)\,\mathrm{d}t \tag{3.5}$$

and

$$\overline{\delta^2_{i,r}(\Delta)} = \frac{1}{T-\Delta}\int_0^{T-\Delta} \delta^2_{i,r}(t,\Delta)\,\mathrm{d}t. \tag{3.6}$$

Then, we take the ensemble average over N trajectories

$$\left\langle \overline{\delta^2(\Delta)} \right\rangle = \frac{1}{N}\sum_{i=1}^{N} \overline{\delta^2_i(\Delta)}. \tag{3.7}$$

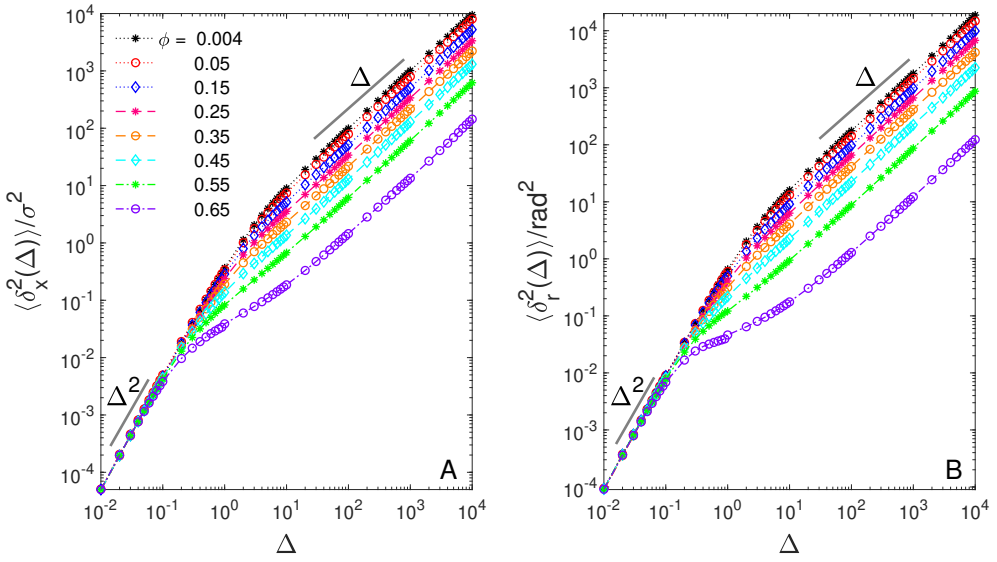

Figure 3.1: (A) Translational and (B) rotational mean time-averaged MSD of the centre of mass of the dumbbell-shaped crowder for varying packing fractions ϕ. Parameters: the inter-particle attraction strength is $\epsilon = 1k_BT$, the trace length $T = 5 \cdot 10^5 \delta\tau \approx 0.5\,\mathrm{ms}$. The mean $\left\langle \overline{\delta^2(\Delta)} \right\rangle$ is computed over $N = 40$ trajectories. The lag time Δ in these and the following plots is given in units of $\delta\tau \approx 1\,\mathrm{ns}$.

Figure 3.1 shows the translational and rotational time-averaged MSDs against the lag time Δ for varying crowding fractions ϕ. Three different behaviours can be distinguished. Initially for $\Delta < 0.1\delta\tau$, the diffusion is ballistic. The MSD appears the same for all ϕ. The ballistic regime is typical for the motion of inertial particles, see figure 7.1. Travelling only a fraction of σ, the motion of the dimers is not yet hindered by collisions with neighbouring crowders. In the ballistic regime, the displacement grows linear which can be interpreted as the dimers moving with a constant velocity. At intermediate lag times $\Delta \sim 0.1 \ldots 10\delta\tau$, a transition occurs. Based on ϕ, the MSDs start to split. This transition is caused by the first collisions between the dimers. In the long time limit the MSD grows linearly with Δ, following standard Brownian diffusion of equation 1.2.

3.1.1 Scaling exponent

To examine the ϕ-dependence of the MSD, the local scaling exponents β_x, β_r are calculated. We use the method of differentiating form [20]

$$\beta_x(\Delta) = \frac{\mathrm{d}\,\log\left(\left\langle \overline{\delta_x(\Delta)^2} \right\rangle\right)}{\mathrm{d}\,\log(\Delta)} \tag{3.8}$$

and

$$\beta_r(\Delta) = \frac{\mathrm{d}\log\left(\left\langle\overline{\delta_r(\Delta)^2}\right\rangle\right)}{\mathrm{d}\log(\Delta)}. \tag{3.9}$$

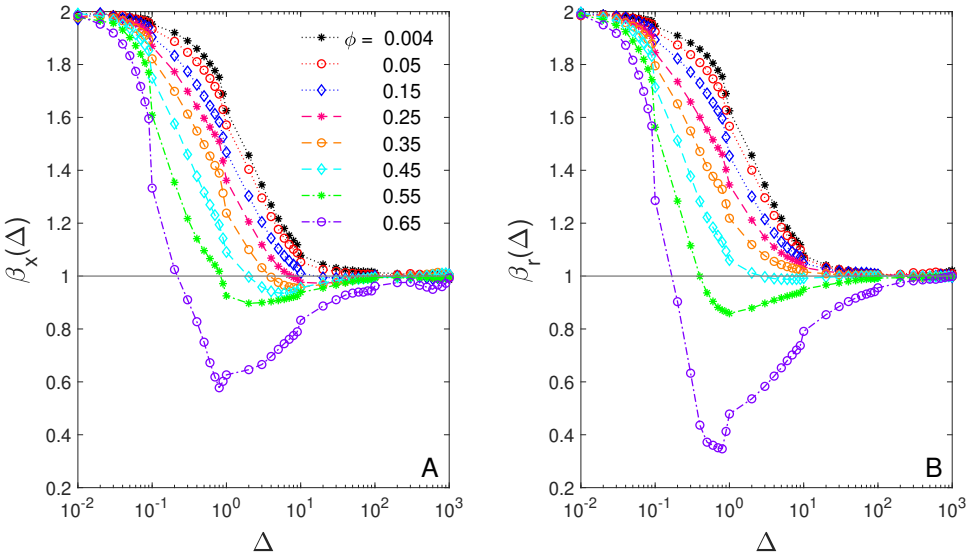

Figure 3.2: (A) Translational and (B) rotational local scaling exponent for varying packing fractions ϕ.

As seen in figure 3.2, crowding has a profound impact on the intermediate behaviour of the scaling exponent which starts earlier as anticipated from figure 3.1. In contrast, the scaling exponent is initially 2 for all ϕ and at long times β_x and β_r tend to 1 for all crowding fractions. The linear and rotational motion are fully correlated. We observe subdiffusive values of β_x and β_r for the most crowded systems. The subdiffusion is more pronounced for the rotation. In the more diluted systems the transition from the ballistic to the linear regime follows standard Brownian diffusion, compare figure 7.1.

3.1.2 Diffusivity

In the long-time limit, β_x and β_r are not ϕ-dependent. Thus, the long-time ϕ-dependence of the MSD must stem from the diffusivities which can be evaluated by

$$D_x = \frac{\left\langle\overline{\delta_x(\Delta)^2}\right\rangle}{2\Delta} \tag{3.10}$$

and

$$D_r = \frac{\left\langle\overline{\delta_r(\Delta)^2}\right\rangle}{2\Delta}. \tag{3.11}$$

Using a linear fit of the MSD in the range $\Delta = 10^2 \dots 10^4$, the diffusivity is obtained by the slope of the fit divided by 2.

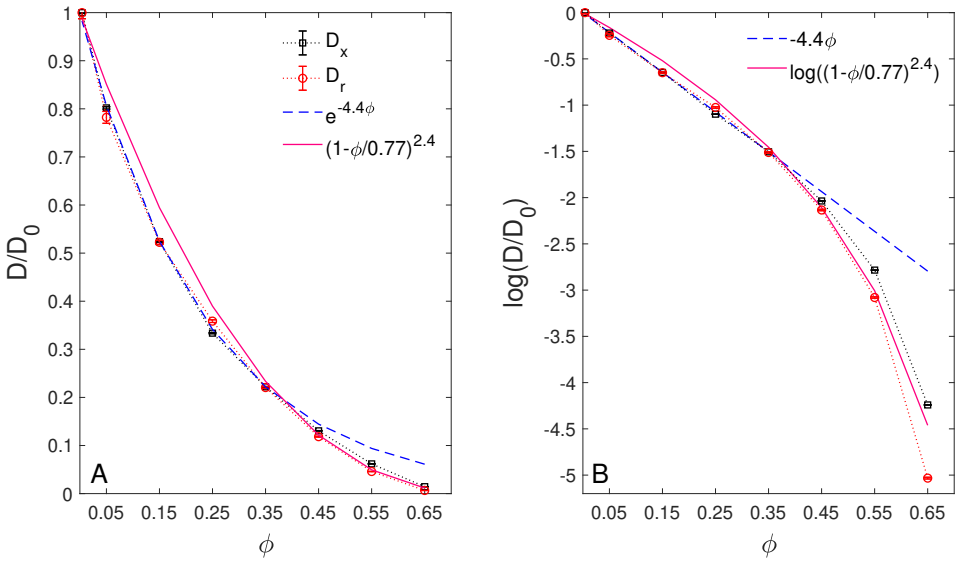

Figure 3.3: A: Normalised long-time translational and rotational diffusivity as a function of the crowding fraction ϕ together with an exponential decay fit for small ϕ and a quadratic fit for large ϕ. $D_0 = D(\phi = 0.004)$. The normalisation is with respect to $D_0 = D(\phi = 0.004)$. B: Lin-log plot of the data and fits from A.

Figure 3.3 shows the normalised translational and rotational diffusivities as functions of the crowding fraction ϕ. Both diffusivities display similar behaviour. For small ϕ, the diffusivity decays exponentially, see figure 3.3 B, as suggested in [21] for crowded liquids. For large ϕ, however, we see a different dependence in figure 3.3 B. A power-law dependence of the diffusivity was shown in [22] for a system of polydisperse hard disks with a glass transition

$$D(\phi) \propto (\phi - \phi^*)^{2.4}. \tag{3.12}$$

Here ϕ^* is the crowding fraction at which the glass transition occurs. In figure 3.3 we plot these two dependencies as the best fits to their respective ranges of ϕ. A power law with $\phi^* \approx 0.77$ provides the best fit to our data. The crossover from exponential to power-law dependence is located between 0.35 and 0.45. The same range at which the subdiffusion starts to occur in 3.2.

3.2 Displacement probability density function

The displacement PDFs $p(\delta_x)$ and $p(\delta_r)$ are obtained by sorting the displacements and weighting each displacement with the same probability. We calculate the PDFs for $\Delta = 0.1 \ldots 80\delta\tau$.

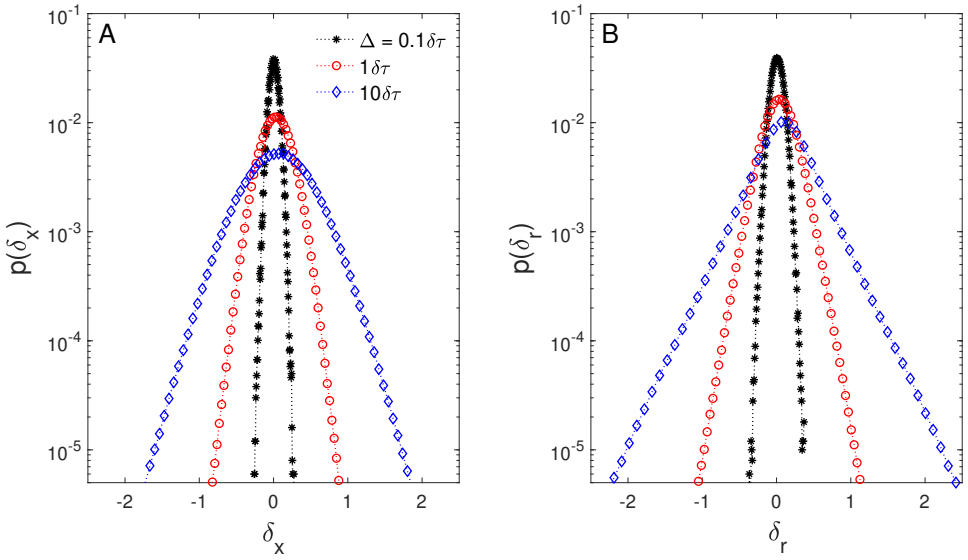

Figure 3.4: (A) Translational and (B) rotational displacement PDF for $\phi = 0.65$ at various lag times Δ.

The translational and rotational displacement PDFs are plotted in figure 3.4 for the highest crowding fraction $\phi = 0.65$. At $\Delta = 0.1\delta\tau$ both PDFs have the same parabolic shape. However, with longer times the shapes of the PDFs differ. While the translational PDF remains its parabolic shape the rotational PDF becomes triangular. The parabolic shape is a characteristic feature of lin-log plot of a Gaussian PDF. Another shape indicates a non-Gaussian PDF.

3.2.1 Non-Gaussian parameter

To asses the shape of the PDF we use the non-Gaussian parameter G which is closely related to the kurtosis

$$G_x = \frac{\mathrm{Kurt}[\delta_x]}{3} - 1 = \frac{\langle \delta_x^4 \rangle}{3(\langle \delta_x^2 \rangle - \langle \delta_x \rangle^2)^2} - 1. \tag{3.13}$$

Here $\langle \delta_x \rangle$, $\langle \delta_x^2 \rangle$ and $\langle \delta_x^4 \rangle$ represent the first, second and fourth moment of δ_x, respectively. G_r is defined analogously.

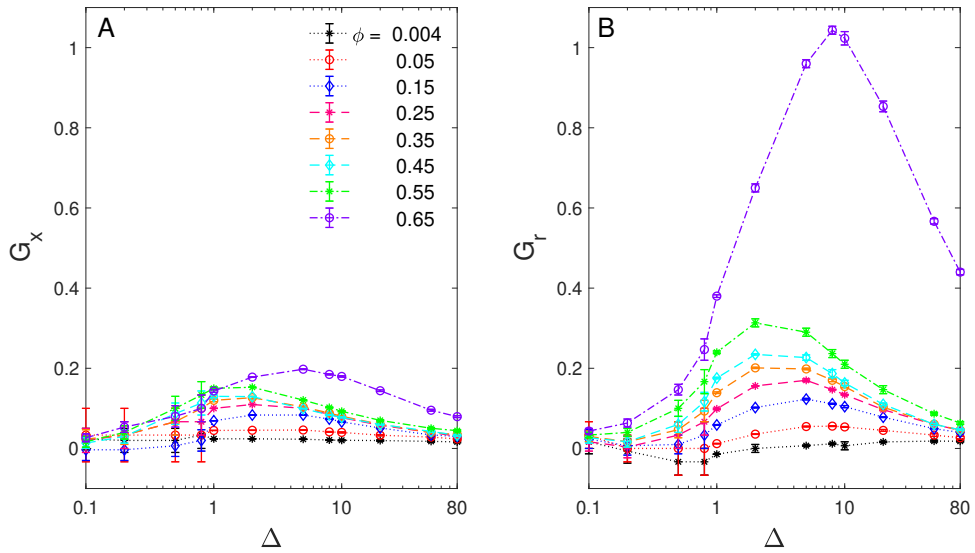

Figure 3.5: (A) Translational and (B) rotational non-Gaussian parameter plotted against lag time Δ for various packing fractions ϕ.

Figure 3.5 shows the lag time dependence of the non-Gaussian parameter for various ϕ. Initially, the PDFs are Gaussian as G_x, $G_r \sim 1$. Then, G_x, G_r increase and reach a maximum at intermediate times. Approaching lag times of the standard Brownian diffusion, G tends to 0 again. The most pronounced deviation from the Gaussian G of 0 occurs for $\phi = 0.65$. The maximal translational non-Gaussian parameter is ~ 0.2. The maximum of G_r exceeds 0.2 significantly. It reaches ~ 1, indicating a Laplacian PDF.

3.2.2 Second moment

To investigate if 1.5 holds also for non-Gaussian PDFs, we evaluate the second moment $\langle \delta_x^2 \rangle$ of the displacement PDF by

$$\langle \delta_x^2 \rangle = \int_{\infty}^{\infty} \delta_x^2 \, p(\delta_x) \, \mathrm{d}\delta_x \tag{3.14}$$

and analogously for the rotational displacement PDF.

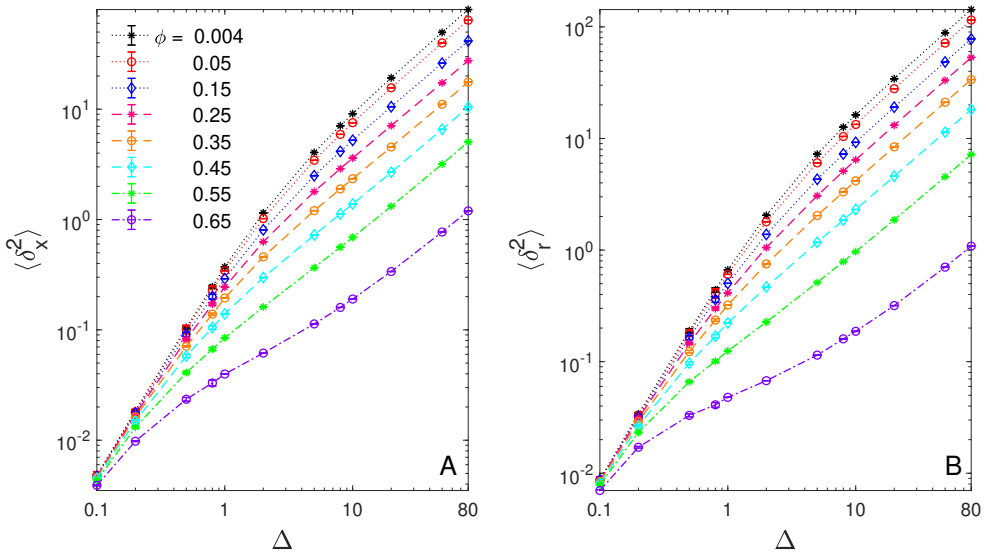

Figure 3.6: Second moment of the (A) translational and (B) rotational displacement PDF as a function of lag time Δ for varying packing fractions ϕ.

Figure 3.6 shows the lag time dependence second moment of the translational and rotational displacement PDFs for various ϕ. The second moment displays the same behaviour as the time-averaged MSD in the range of $\Delta = 0.1 \ldots 80$.

3.3 Displacement autocorrelation function

As a third approach, we evaluate the displacement/velocity autocorrelation function C_x for the translational displacement δ_x, the rotational displacement δ_r and the displacement of the relative coordinate δ_r. With the time difference between two displacements τ, the autocorrelation is obtained by

$$C_x(\tau, \Delta) = \overline{v_x(\tau, \Delta) v_x(0, \Delta)} = \frac{1}{T - \Delta - \tau} \int_0^{T-\Delta-\tau} \frac{\delta_x(t+\tau, \Delta)\delta_x(t, \Delta)}{\Delta^2} \, \mathrm{d}t. \tag{3.15}$$

Here Δ is a fixed value of the lag time. The factor $1/\Delta^2$ stems from the definition of the velocity

$$v_x(t) = \frac{\Delta x}{\Delta t} = \frac{x(\Delta + t) - x(t)}{t + \Delta - t} = \frac{\delta(t, \Delta)}{\Delta}. \tag{3.16}$$

In the following, we call τ outer and Δ inner lag time. C_r and C_d are calculated analogously.

3.3.1 Translation and rotation

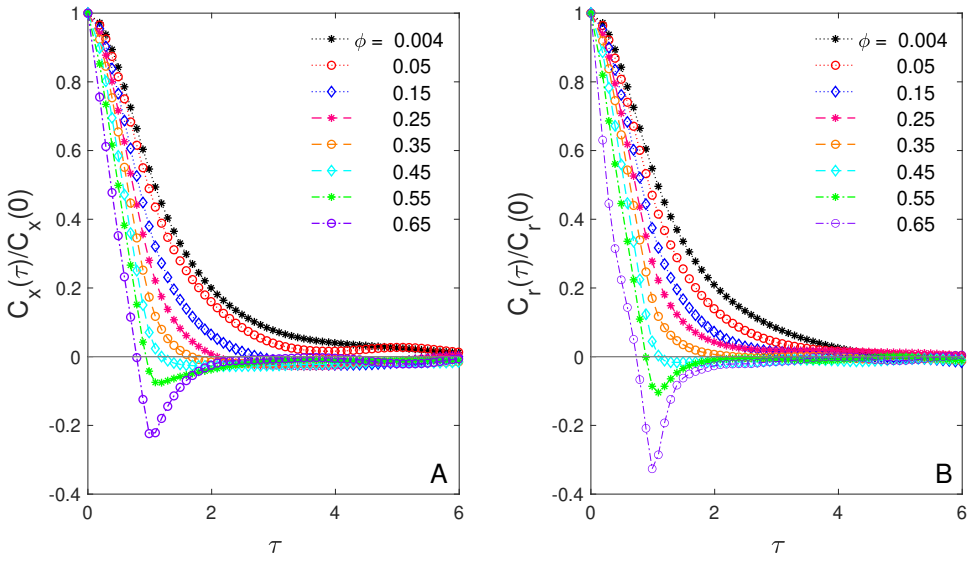

Figure 3.7: Normalised (A) translational and (B) rotational displacement autocorrelation function as a function of the outer lag time τ for varying crowding fractions ϕ, with $C(0) = \overline{v_k(0)^2}$. Parameter: the inner lag time is $\Delta = 1\delta\tau$.

In figure 3.7, we present the translational and rotational displacement autocorrelation function plotted against the outer lag time for varying ϕ. In general, C_x and C_r decay to zero. The decay rate depends on ϕ. For small crowding fractions, this decay is monotone while for the most crowded systems C_x and C_r display non-monotonic behaviour with a minimum at $\tau = \Delta$. These anticorrelations indicate a reversal of the motion.

3.3.2 Relative coordinate

The normalised displacement autocorrelation function of the relative coordinate is plotted against the outer lag time for $\phi = 0.004$ in figure 3.8. The oscillations of C_d indicate the vibration of the dimer and the exponentially decaying amplitude the damping due to the environment. With increasing ϕ the damping also increases to the point where the oscillation is almost completely suppressed, see figures 7.3 to 7.6. The ϕ dependence of α is plotted in figure 3.9. To show the similarity of the behaviour compared to the diffusivity, the inverse normalised decay constant is shown. Like the diffusivity, α depends exponentially on ϕ. Only for the most crowded case we observe deviations from the exponential behaviour.

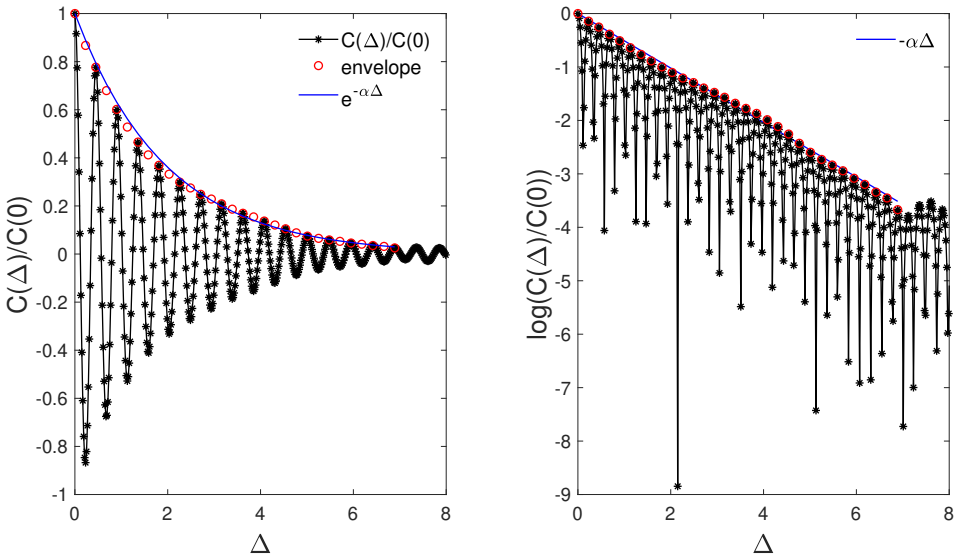

Figure 3.8: A: Normalised displacement autocorrelation function of the relative coordinate as a function of lag time τ for $\phi = 0.004$. The amplitude of the correlation function is plotted as an envelope together with an exponential decay fit. B: Data from A in a lin-log plot together with a linear plot indicating the exponential decay from A. The inner lag time is $\Delta = 0.1\delta\tau$

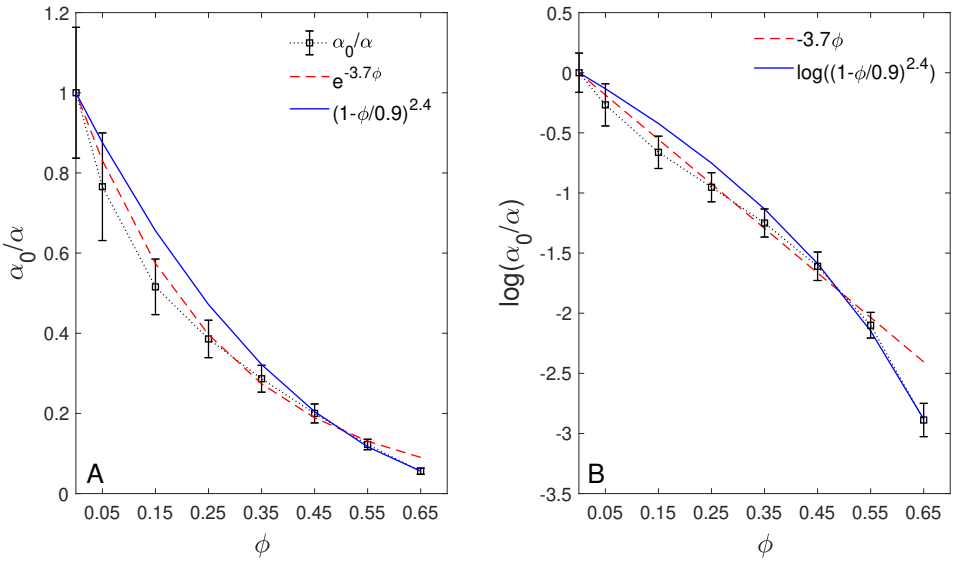

Figure 3.9: The normalised inverse decay constant as a function of the crowding fraction ϕ.

4 Discussion

Based on our results, the range of crowding fractions can be divided into two regimes. First, for low ϕ (≤ 0.35) we observe standard Brownian diffusion in the form of the scaling exponent 3.2 and the displacement correlation function 3.7. In this regime, the crowding can be modelled as an effective damping constant γ_{eff}, compare figures 3.2 and 7.1. Using equation 1.3, $\gamma_{\text{eff}(\phi)}$ can be obtained form figure 3.3 and, as the diffusivity, $1/\gamma_{\text{eff}}$ depends exponentially on ϕ. Second, the subdiffusive scaling exponent and the displacement correlation function that displays anticorrelations indicate anomalous diffusion for high ϕ (>0.35). In this regime, the diffusivity decreases as a power law with ϕ. A model that combines subdiffusion and anticorrelation is the anti-persistent fractional Brownian motion (FBM) [23] as well as the related model of a motion governed by a fractional Langevin equation without an external potential [24].

These models are associated with motion in viscoelastic environments [9, 25]. Thus, we interpret the two regimes of crowding as a viscous liquid for low ϕ and as a viscoelastic liquid for high ϕ. A concentration-dependent transition between viscous and viscoelastic diffusion was also proposed in [26]. We also observed this transition for the diffusion of single unconnected monomers characterised by the crossover of the diffusivity dependencies, see figure 7.2. Here, the transition occurs for higher ϕ as only the Lennard-Jones potential can be the source of the elasticity. This comparison suggests that more complex crowders such as a linear chain of three monomers should exhibit the transition at smaller ϕ.

To further discuss the effect the dumbbell shape has on the diffusion, we highlight key differences of our results compared to the results of the study of the diffusion of star-shaped crowders. For the latter, transient subdiffusion occurs for all crowding fractions, while only the most crowded dimer systems exhibit such behaviour. Similarly, the power law dependence of the diffusivity was observed in [1] for all ϕ while we observe this dependence only in the high ϕ cases. Moreover, the crowding fraction of the glass transition ϕ^* is smaller for the star-shaped crowders than for the dumbbell-shaped crowders, ~ 0.52 and ~ 0.77, respectively.

These deviations can be traced back to different structures of the two crowders. The inner monomer of the star, of which the movement is tracked, is connected to the three other monomers by elastic springs. Thus, the environment of the inner monomer is always, independently of the crowding, viscoelastic. In contrast, a monomer is only connected to one other monomer, allowing for a viscous environment at low ϕ. The difference in ϕ^* between the two crowders can be explained by the simpler structure of

the dimer felicitating a more dense packing before the glass transition occurs.

The damped-oscillating displacement autocorrelation, as we observe for the relative coordinate, is typical for the standard Brownian motion of a harmonic oscillator [27], see figure 7.6 B. This similarity is to be expected as equation 2.3 reduces to the Langevin equation of a randomly driven harmonic oscillator when only a single dimer is considered. In this diluted case, the Lennard-Jones interaction can be neglected as the distance between the two monomers is $\sim r_0$. In addition, [27] gives a meaning to the decay constant $\alpha = \gamma/(2m)$. To preserve this relation, we again use the effective crowding constant $\gamma_{\text{eff}(\phi)}$. Hence, the vibration of the dimer can be modelled as the oscillation of a randomly driven harmonic oscillator with a crowding dependent effective damping constant. Similar to the diffusivity, α decreases exponentially with ϕ in this regime of standard Brownian diffusion. The deviation from this behaviour at large ϕ indicates another diffusion regime. Due to the worse accuracy of the data of α, however, the transition is not as clear. This regime might be modelled by a motion governed by a fractional Langevin equation with an external harmonic potential [12].

5 Conclusion

We simulated the diffusion of simple linear crowders and performed data analysis of the measured observables. Our crowders consist of two monomers connected by an harmonic potential allowing the dimer to vibrate. In addition, we implemented a weak inter-crowder attraction.

We found two distinct diffusion regimes. For diluted systems, we found standard Brownian diffusion with a Gaussian displacement PDFs and a exponentially decaying displacement autocorrelation function. The effect of ϕ on the diffusion is modelled as an effective damping. The damping is obtained from the diffusivity which decreases exponentially with ϕ in this regime. Similarly, the damping of the vibration of the dimers depends exponentially on ϕ. For highly crowded systems, we found transient subbdiffusion, non-Gaussian PDFs and anticorrelated displacements. In this regime, the diffusivity decreases like a power law with increasing ϕ. Some of these aspects might be modelled by fractional Langevin equations.

We attribute the two different regimes to the crowding induced transition from a viscous liquid to a viscoelastic liquid. To verify this hypothesis, further studies could include the crowding dependence of the average inter-monomer forces or the number of interacting neighbours, combining crowding and structure in a single quantity, as well as crowders made up of three monomers in different shapes, e.g. linear and triangular. A Bayesian analysis could determine the involved diffusion models [28]. In the end, predictions of the diffusion properties based on the physical properties of the environment of a simple crowder particle might be possible.

Acknowledgements

I sincerely thank Ralf Metzler and Andrey Cherstvy for their consultation on the choice of the topic as well as their guidance for the data analysis. Also, I would like to thank Andrey Cherstvy for the additional material on the topic that he provided. This study would not have been possible without the integral support and advice of Jeaoh Shin on the simulation. Furthermore, I thank Samudrajit Thapa for the orientation he provided in the early phase of this thesis and Yousof Mardoukhi for his technical support. Last but not least, I thank Leif Peters for our constructive and motivating discussions.

6 References

[1] Jeaoh Shin, Andrey G. Cherstvy, and Ralf Metzler. "Self-subdiffusion in solutions of star-shaped crowders: non-monotonic effects of inter-particle interactions". In: *New Journal of Physics* 17.11 (2015), p. 113028. DOI: 10.1088/1367-2630/17/11/113028.

[2] Robert Brown. "A brief account of microscopical observations made in the months of June, July and August 1827, on the particles contained in the pollen of plants; and on the general existence of active molecules in organic and inorganic bodies". In: *The Philosophical Magazine* 4.21 (1828), pp. 161–173. DOI: 10.1080/14786442808674769.

[3] Albert Einstein. "Über die von der molekularkinetischen Theorie der Wärme geforderte Bewegung von in ruhenden Flüssigkeiten suspendierten Teilchen". In: *Annalen der Physik* 322.8 (1905), pp. 549–560. DOI: 10.1002/andp.19053220806.

[4] Marian von Smoluchowski. "Zur kinetischen Theorie der Brownschen Molekularbewegung und der Suspensionen". In: (Jan. 1906). DOI: 10.1002/andp.19063261405.

[5] Paul Langevin. "Sur la théorie du mouvement brownien". In: *Comptes rendus de l'Académie des sciences* 146 (1908), pp. 530–533.

[6] Xin Bian, Changho Kim, and George Em Karniadakis. "111 years of Brownian motion". In: *Soft Matter* 12 (30 2016), pp. 6331–6346. DOI: 10.1039/C6SM01153E. URL: http://dx.doi.org/10.1039/C6SM01153E.

[7] Julia F. Reverey et al. "Superdiffusion dominates intracellular particle motion in the supercrowded cytoplasm of pathogenic Acanthamoeba castellanii". In: *Scientific Reports* 5 (1 2015), pp. 2045–2322. DOI: 10.1038/srep11690.

[8] Ido Golding and Edward C. Cox. "Physical Nature of Bacterial Cytoplasm". In: *Phys. Rev. Lett.* 96 (9 2006), p. 098102. DOI: 10.1103/PhysRevLett.96.098102.

[9] Ralf Metzler, Jae-Hyung Jeo, Andrey G. Cherstvy, and Eli Barkai. "Anomalous diffusion models and their properties: non-stationarity, non-ergodicity, and ageing at the centenary of single particle tracking". In: *Phys. Chem. Chem. Phys.* 16 (44 2014), pp. 24128–24164. DOI: 10.1039/C4CP03465A.

[10] I. M. Sokolov, E. Heinsalu, P. Hänggi, and I. Goychuk. "Universal fluctuations in subdiffusive transport". In: *EPL (Europhysics Letters)* 86.3 (2009), p. 30009. DOI: 10.1209/0295-5075/86/30009.

[11] Benoit B. Mandelbrot and John W. Van Ness. "Fractional Brownian Motions, Fractional Noises and Applications". In: *SIAM Review* 10.4 (1968), pp. 422–437. DOI: 10.1137/1010093.

[12] Trifce Sandev, Ralf Metzler, and Živorad Tomovski. "Correlation functions for the fractional generalized Langevin equation in the presence of internal and external noise". In: *Journal of Mathematical Physics* 55.2 (2014), p. 023301. DOI: 10.1063/1.4863478.

[13] Jae-Hyung Jeon, Aleksei V. Chechkin, and Ralf Metzler. "Scaled Brownian motion: a paradoxical process with a time dependent diffusivity for the description of anomalous diffusion". In: *Phys. Chem. Chem. Phys.* 16 (30 2014), pp. 15811–15817. DOI: 10.1039/C4CP02019G.

[14] Andrey G. Cherstvy, Aleksei V. Chechkin, and Ralf Metzler. "Anomalous diffusion and ergodicity breaking in heterogeneous diffusion processes". In: *New Journal of Physics* 15.8 (2013), p. 083039. DOI: 10.1088/1367-2630/15/8/083039.

[15] Francesco Sciortino and Piero Tartaglia. "Glassy colloidal systems". In: *Advances in Physics* 54.6-7 (2005), pp. 471–524. DOI: 10.1080/00018730500414570.

[16] Jaeoh Shin, Andrey G. Cherstvy, and Ralf Metzler. "Kinetics of polymer looping with macromolecular crowding: effects of volume fraction and crowder size". In: *Soft Matter* 11 (3 2015), pp. 472–488. DOI: 10.1039/C4SM02007C.

[17] Michael P. Allen and Dominic J. Tildesley. *Computer simulations of liquids*. Oxford: Clarendon, 1987.

[18] Wendy A. Bickmore and Heidi G. E. Sutherland. "Addressing protein localization within the nucleus". In: *The EMBO Journal* 21.6 (2002), pp. 1248–1254. DOI: 10.1093/emboj/21.6.1248.

[19] URL: https://github.com/bachelorphysic/Simulation-.git.

[20] Alexander M. Berezhkovskii, Leonardo Dagdug, and Sergey M. Bezrukov. "Discriminating between Anomalous Diffusion and Transient Behavior in Microheterogeneous Environments". In: *Biophysical Journal* 106.2 (2014), pp. L09–L11. DOI: https://doi.org/10.1016/j.bpj.2013.12.013.

[21] Ronald J. Phillips. "A Hydrodynamic Model for Hindered Diffusion of Proteins and Micelles in Hydrogels". In: *Biophysical Journal* 79.6 (2000), pp. 3350–3353. DOI: https://doi.org/10.1016/S0006-3495(00)76566-0.

[22] Ludger Santen and Werner Krauth. "Absence of thermodynamic phase transition in a model glass former". In: *Nature* 405 (2000), pp. 550–551. DOI: 10.1038/35014561.

[23] Evangelos Bakalis, Siegfried Höfinger, Alessandro Venturini, and Francesco Zerbetto. "Crossover of two power laws in the anomalous diffusion of a two lipid membrane". In: *The Journal of Chemical Physics* 142.21 (2015), p. 215102. DOI: 10.1063/1.4921891.

[24] Trifce Sandev, Ralf Metzler, and Živorad Tomovski. "Velocity and displacement correlation functions for fractional generalized Langevin equations". In: *Fractional Calculus and Applied Analysis* 15.3 (2012), pp. 426–450. DOI: doi:10.2478/s13540-012-0031-2.

[25] Matthias Weiss. "Single-particle tracking data reveal anticorrelated fractional Brownian motion in crowded fluids". In: *Phys. Rev. E* 88 (1 2013), p. 010101. DOI: 10.1103/PhysRevE.88.010101.

[26] J. S. Vrentas and C. M. Vrentas. "Viscoelastic diffusion". In: *Journal of Polymer Science Part B: Polymer Physics* 39.13 (2001), pp. 1529–1547. DOI: https://doi.org/10.1002/polb.1126.

[27] Ming Chen Wang and G. E. Uhlenbeck. "On the Theory of the Brownian Motion II". In: *Rev. Mod. Phys.* 17 (2-3 1945), pp. 323–342. DOI: 10.1103/RevModPhys.17.323.

[28] Samudrajit Thapa, Michael A. Lomholt, Jens Krog, Andrey G. Cherstvy, and Ralf Metzler. "Bayesian analysis of single-particle tracking data using the nested-sampling algorithm: maximum-likelihood model selection applied to stochastic-diffusivity data". In: *Phys. Chem. Chem. Phys.* 20 (46 2018), pp. 29018–29037. DOI: 10.1039/C8CP04043E.

7 Appendix

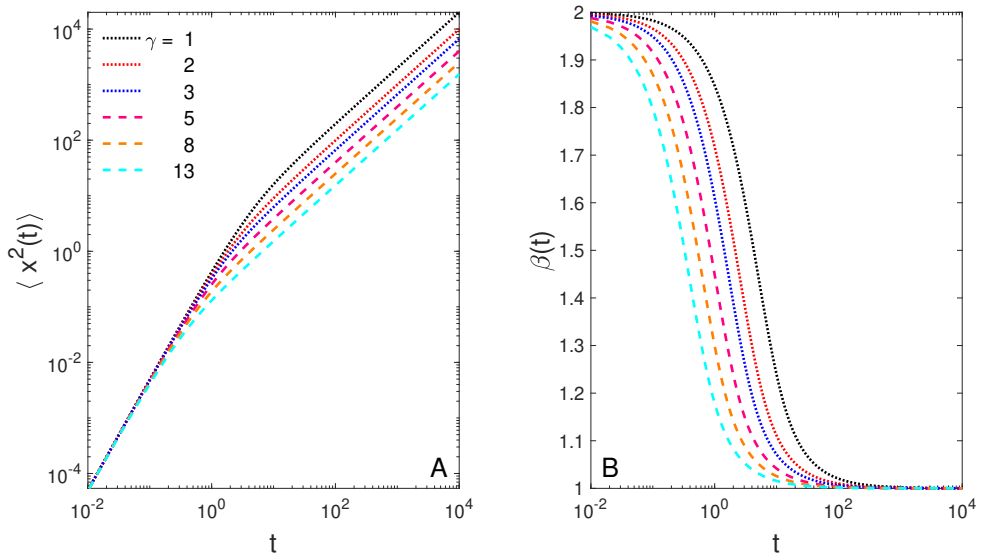

Figure 7.1: A: MSD of the motion governed by equation 1.4 (equation (17) from [6]) for varying damping constants, with $k_BT = 1$ and $m = 1$. B: Scaling exponent of the MSD from A, calculated by equation 3.8.

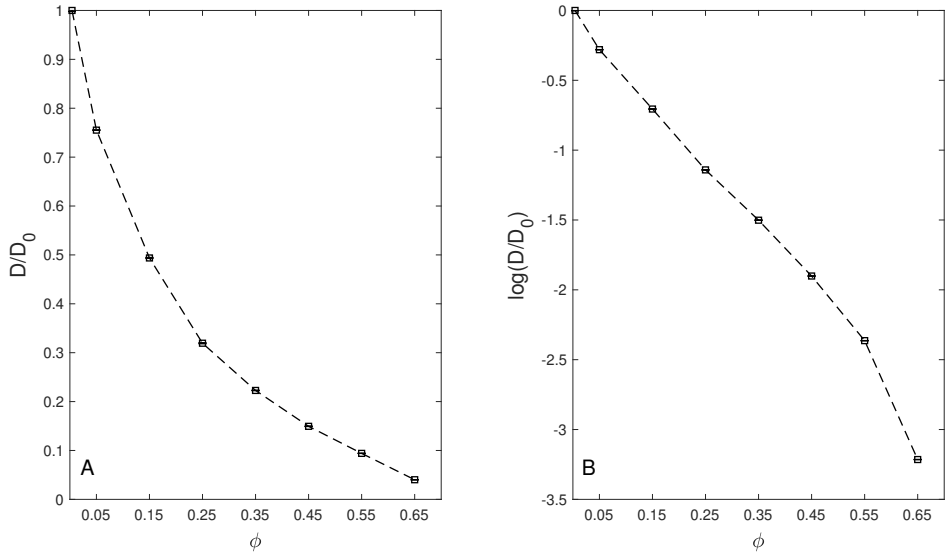

Figure 7.2: A: Translational diffusivity as a function of ϕ. Obtained by 3.10 from the MSD of the diffusion of single unconnected monomers. B: Lin-log plot of the data of A. Parameters are the same as in 3.1.

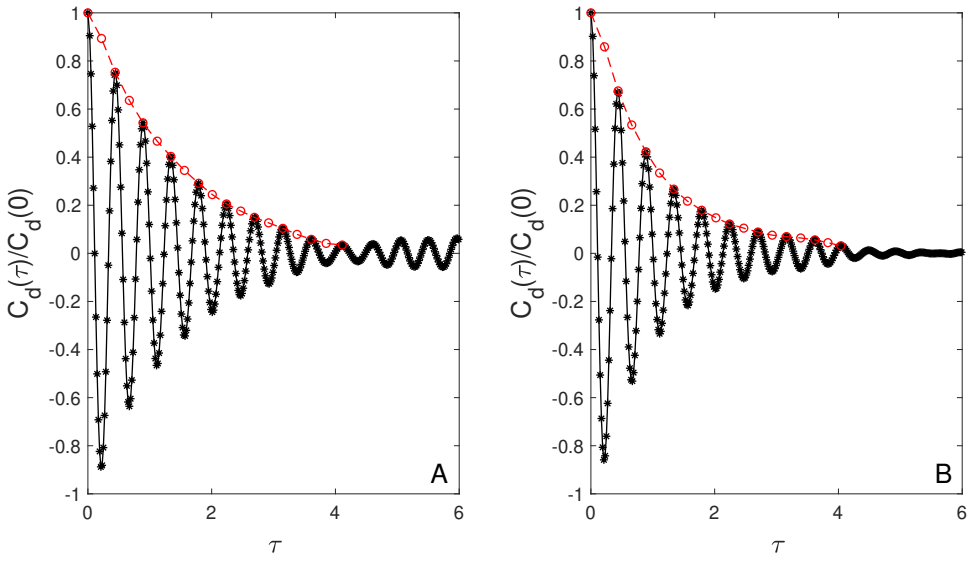

Figure 7.3: Displacement autocorrelation function of the relative coordinate for (A) $\phi = 0.05$ and (B) $\phi = 0.15$. The red circles are the amplitudes in the following plots.

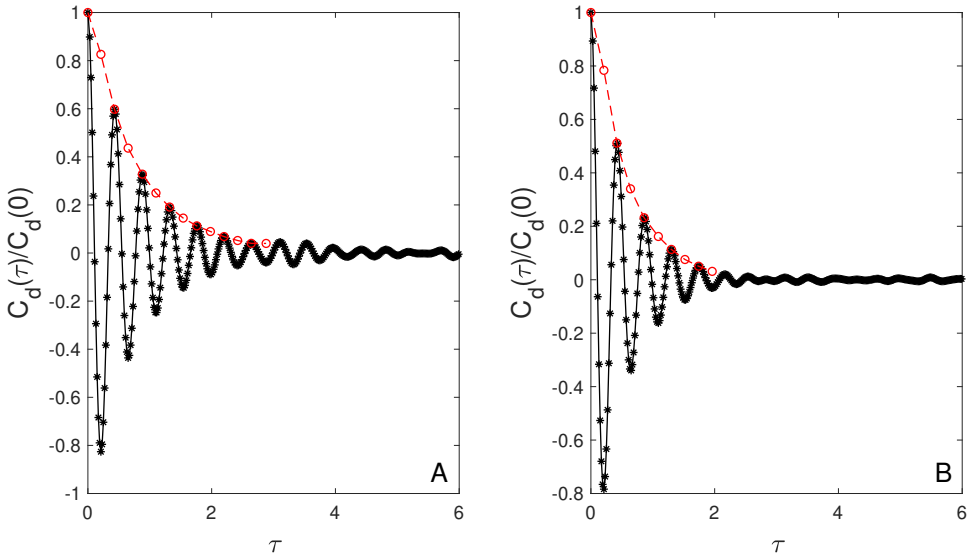

Figure 7.4: Displacement autocorrelation function of the relative coordinate for (A) $\phi = 0.25$ and (B) $\phi = 0.35$.

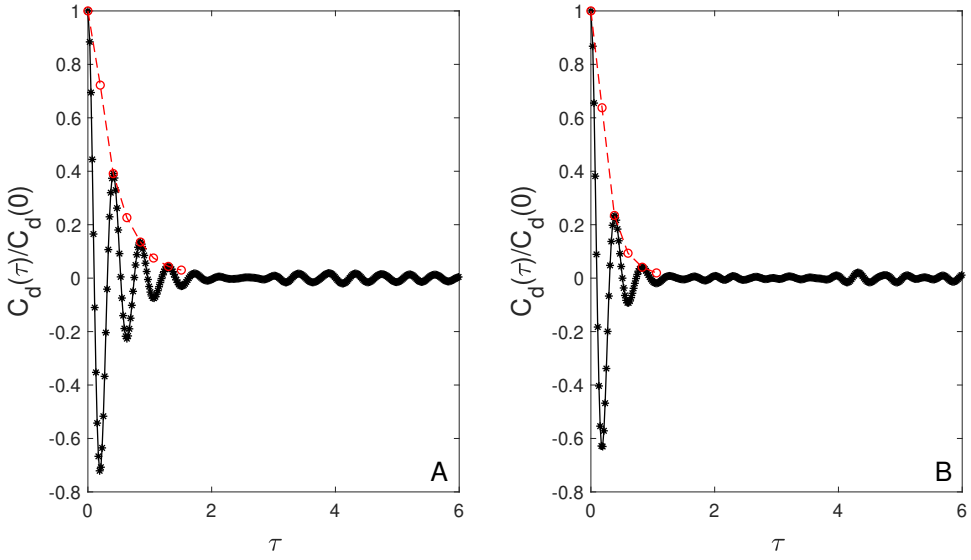

Figure 7.5: Displacement autocorrelation function of the relative coordinate for (A) $\phi = 0.45$ and (B) $\phi = 0.55$.

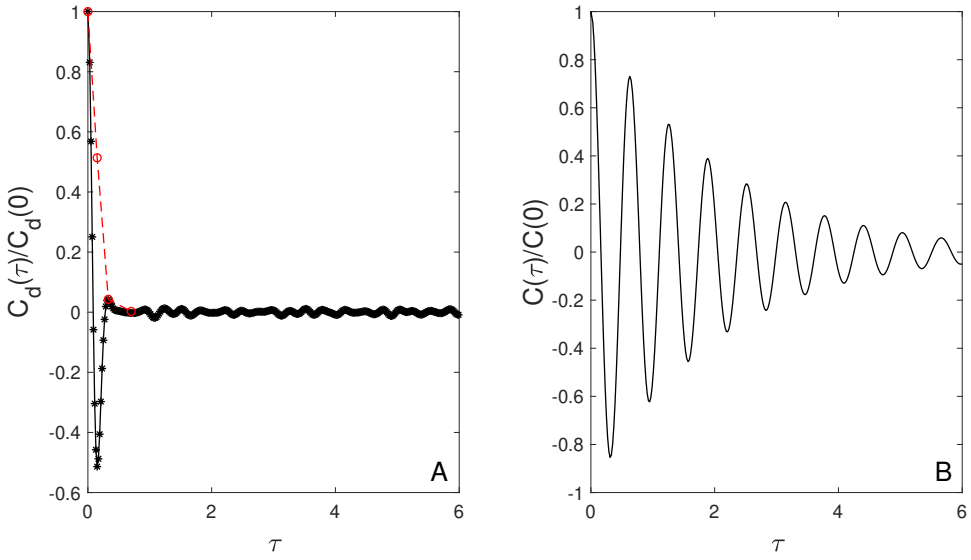

Figure 7.6: A: Displacement autocorrelation function of the relative coordinate for $\phi = 0.65$. B: Normalised displacement autocorrelation function for the Brownian motion of a harmonic oscillator (equation (50a) from [27]) with parameters $\omega_0 = 10$ and $\beta = 1$.